Journal of Applied Fluid Mechanics, Vol. 17, No. 2, pp. 384-397, 2024.
Available online at www.jafmonline.net, ISSN 1735-3572, EISSN 1735-3645.
https://doi.org/10.47176/jafm.17.02.2106

Effect of Obstacle Length Variation on Hydrogen Deflagration in a Confined Space Based on Large Eddy Simulations

B. Ai[1,2], J. Gao[1,3,4†], B. Hao[1], B. Guo[1] and J. Liang[5]

[1] *School of Petrochemical Engineering & Environment, Zhejiang Ocean University, Zhoushan, 316022, China*
[2] *School of Naval Architecture & Maritime, Zhejiang Ocean University, Zhoushan, 316022, China*
[3] *National & Local Joint Engineering Research Center of Harbor Oil & Gas Storage and Transportation Technology, Zhoushan, 316022, China*
[4] *Zhejiang Key Laboratory of Petrochemical Environmental Pollution Control, Zhoushan, 316022, China*
[5] *Department of Oil, Army Logistical University, Chongqing, 401331, China*

†*Corresponding Author Email: gaojf309@126.com*

ABSTRACT

In the field of hydrogen safety and combustion, the effect of obstacles on hydrogen deflagration is a topic of general interest to scholars. In previous studies, scholars usually used uniform obstacles under various operating conditions and obtained conclusions by changing their number and positions. However, in practice, the shapes of obstacles at an accident site are often not the same and regular. In this paper, a series of obstacles with variations in length were investigated, and the effects of the obstacles on hydrogen deflagration under different working conditions were analyzed. The configuration of the obstacles with gradually increasing lengths amplified the vortices in the flow field so that the propagation direction of the flame front surface was reversed after passing three obstacles. The variations in the lengths of the obstacles had a significant stretching effect on the propagation of the flame and a considerable acceleration effect on the propagation speed of the flame. The main reason for the acceleration was the rapid propagation of the flame achieved by the vortex when rupture occurred. The change in the pressure gradient that occurred at the center of rotation caused rapid movement of the combustion gases, which ultimately led to an increase in the flame propagation speed. A configuration with gradually increasing lengths of the obstacles promoted the overpressure. A configuration with gradually decreasing lengths of the obstacles suppressed the overpressure. The reason for the formation of the local high-pressure area was that unburned gas was accumulated there by pressure waves and the obstacle walls, and then the thermal expansion formed a high pressure. The Rayleigh–Taylor and Kelvin–Helmholtz instabilities caused the overpressure to rise further. The results can provide a theoretical basis for hydrogen transportation, storage, and safety.

Article History

Received June 15, 2023
Revised August 24, 2023
Accepted October 5, 2023
Available online December 4, 2023

Keywords:

Explosion and combustion
Flame
Gradient
Obstacle
Vortex

1. INTRODUCTION

In the background of the worldwide struggle to reduce carbon emissions and promote a low-carbon energy transition and energy revolution, some countries and regions are considering the utilization of hydrogen energy to reduce greenhouse gas emissions. Hydrogen has the advantages of a high combustion calorific value and clean combustion products and is an ideal energy carrier for wind, solar, hydroelectric, and other renewable energy sources (Dincer & Acar, 2015; Wang et al., 2022a). As a result, the world's demand for hydrogen energy is predicted to rise significantly in the coming years.

Hydrogen is currently transported by pipeline, rail, truck, and ship (Di Lullo et al., 2022). Through the analysis of existing transportation systems, most scholars believe that large-scale, long-distance pipeline transportation is the most environmentally friendly and economical way to transport hydrogen (Demir & Dincer, 2018; Faye et al., 2022; Zhao et al., 2022). However, although hydrogen has good energy qualities, it is also an extremely flammable and explosive gas with highly active chemical properties, which poses a stern challenge to the transportation and storage of hydrogen.

The occurrence and development of the deflagration of methane, natural gas, liquefied petroleum gas (LPG),

Nomenclature

ρ	density	μ_{sgs}	subgrid viscosity coefficient
t	time	L_s	subgrid-scale mixing length
u	speed	s_{ij}	spin rate tensor component
p	pressure	A_1	first acceleration
τ_{ij}	viscous stress tensor	G_1	growth rate of first acceleration
u_i	velocity components	A_2	second acceleration
u_j	velocity components	G_2	growth rate of second acceleration
h	enthalpy	S_{Max}	maximum speed
λ	thermal conductivity	t_{Max}	time of maximum speed
T	temperature	P_{Max}	maximum overpressure
D	diffusion coefficient	G_{Max_1}	growth rate of maximum overpressure (relative to that with no obstacle)
$\dot{\omega}_c$	normalized chemical reaction rate	t_{max}	time of maximum overpressure
S	heat of chemical reaction	G_{Max_2}	growth rate of maximum overpressure (relative to that in configuration 2)
H	calorific value	s_{ij}	spin rate tensor component

and other combustible gases are closely related to the spatial geometry (Ji et al., 2017; Gong & Li, 2018). A large number of scholars have researched this issue. The blocking rate (BR) is a crucial factor affecting deflagration. It has been found that the flame propagation speed increases and then decreases as the BR of a flat-plate-type obstacle increases in a confined space (Luo et al., 2021). By keeping the BR constant and varying the ratio of the actual area to the effective circulation area, it was found that both the grid type and the perforated disc type achieved the maximum enhancement of the flame speed and overpressure peak (Wang et al., 2022c). In addition, the mechanism of deflagration-to-detonation transition (DDT) varied at different blockage rates. In the range of BR = 0.35–0.5, the excitation waves in the unburned gas formed Mach stems after reflection from the obstacle and the tube wall, and their intensity increased with each obstacle traversed. Eventually, the unburned gas was detonated (Goodwin et al., 2016).

In addition, the shape of the obstacle also affects the flame pattern and overpressure characteristics of combustible gases when deflagration occurs (Hao et al., 2022). During flame propagation, the boundary of the laminar flame is compressed as the flame passes a triangular obstacle. This causes the flame to gather in the center of the tube, which results in the highest turbulence intensity in the tube (Xiao et al., 2022). The angle of obstacle placement has been further studied, and it has been found that the highest overpressure peak is generated when the obstacle angle is 90°. At the same time, an obstacle with the same obstacle angle but with a larger BR reduces the peak of the flame propagation speed (Wen et al., 2017).

Similarly, the position and number of obstacles are also influencing parameters that have been studied by many scholars (Sha et al., 2014; Li et al., 2022c). It has been found that placing obstacles side-by-side or staggered in the center of the pipeline will result in higher flame propagation speeds and overpressures, which should be avoided in actual production (Wen et al., 2013).

In recent years, an increasing number of scholars have been investigating the deflagration phenomenon of hydrogen (Boeck et al., 2016; Ballossier et al., 2021; Korytchenko et al., 2022; Debnath & Pandey, 2023a, b; Zhou et al., 2023). Xiao et al. performed an in-depth study on the deflagration of hydrogen–air premixed gas, analyzed the propagation dynamics of the flame experimentally, and reproduced the process numerically using computational fluid dynamics techniques, such as the large eddy simulation (LES) method. More details about flame propagation within the flow field were captured, revealing the mechanisms of the flow and combustion during flame propagation and the formation mechanisms of special phenomena such as flame backflow and vortices (Xiao et al., 2013; Xiao et al., 2014a, b). Wang et al. kept the BR constant and investigated the effect of a double-channel-type obstacle on hydrogen-doped methane deflagration. This work showed that when the distance between the obstacle and the ignition became larger, the flame propagation speed increased and then decreased, and the fastest propagation speed could be increased to more than five times that under the condition with no obstacles (Wang et al., 2023). Sheng et al. used the same methods to study four obstacles with the same BR but different cross-sectional areas to establish a simplified analytical model of hydrodynamic instability (Sheng et al., 2023). Li et al. used the LES method to compare and analyze the deflagration characteristics of hydrogen and gasoline vapor in a semi-confined tube (Li et al., 2022a). Using the LES method as well, Xu et al. demonstrated through dimensional analysis that the drag coefficient better reflected the effect of the obstacle shape and also presented and validated dimensionless qualitative and quantitative models of the flame propagation speed (Qiming et al., 2022).

However, the obstacles investigated as described above were regular and simple. In actual production, the obstacles that affect the deflagration of combustible gas are often complicated, and it is not easy to classify them as having certain shapes. Therefore, scholars have begun to study obstacles with gradient changes. Such obstacles are often not single in number and tend to change in appearance. Gao et al. analyzed the influence of obstacle height variations on the deflagration of non-uniformly distributed combustible gas and proposed that the

configuration with the rectangular obstacle height decreasing would produce distinct acceleration of the flame. At the same time, when the height of the rectangular obstacle was the same, the overpressure generated by the deflagration was the maximum (Gao et al., 2022). Qin et al. studied the influence of the number of obstacles on the deflation of hydrogen–air premixed gas and performed quantitative analysis of the complex turbulent flame using the fractal theory. The results suggested that the acceleration of the flame was caused by the compression of the flow due to the change of the cross-sectional area in the presence of multiple obstacles (Qin & Chen, 2021). In addition, Qin et al. investigated fence-type obstacles with BRs of 0.37, 0.5, and 0.63(Qin & Chen, 2022). Dai et al. improved the experiments by increasing the number of fence-type obstacles, allowing obstacles with different BRs to exist in a tube and creating a gradient in the BR, which was simulated using the LES method (Dai et al., 2021).

In conclusion, in the field of hydrogen safety and combustion, the effect of obstacles on hydrogen deflagration is a topic of general interest to scholars. Most of the previous studies revolved around regular, simple obstacles, but in practice, obstacles often have a tendency to vary in shape. Studies of obstacles with variations have been relatively rare, especially in the field of hydrogen deflagration. Therefore, in this study, an obstacle with variations was examined, and its influences on the flame structure, flame propagation process, overpressure characteristics, and flow field of hydrogen deflagration were analyzed. The LES method was used to compare and analyze the hydrogen deflagration phenomena under different configurations. The research results can provide a theoretical basis for the prevention and management of hydrogen explosions in narrow spaces, such as various types of pipe corridors, provide reference suggestions for the placement of various types of equipment and facilities, and provide guidance for the actual occurrence and development of hydrogen explosion accidents.

2. NUMERICAL MODEL

In the LES method, vortices smaller than a grid cell are simulated using a model, and vortices larger than a grid cell are computed directly, resulting in smaller errors. Much of the previous literature also proved that the LES method yields better simulation results for the hydrogen deflagration phenomenon (Brennan et al., 2009; Hong et al., 2015; Elshimy et al., 2021; Li et al., 2022d; Shen et al., 2023). The simulation model of the deflagration of combustible gas using the LES method has been introduced in many papers (Liu & Wang, 2022; Pan et al., 2022b), and the combustion model can be found in the literature (Li et al., 2022a).

The LES method applies Favre filtering to small-scale turbulence pulsations and only calculates large-scale turbulence. The calculation amount of the LES method is smaller than that of the DNS method, and the spatial resolution of the LES method is higher than that of the RANS method, which is suitable for the field of combustible gas deflagration. The equations of LES are as follows:

$$\frac{\partial \rho}{\partial t}+\frac{\partial\left(\rho \tilde{u}_j\right)}{\partial x_j}=0, \tag{1}$$

$$\frac{\partial\left(\rho \tilde{u}_j\right)}{\partial t}+\frac{\partial\left(\rho \tilde{u}_i \tilde{u}_j\right)}{\partial x_j}=\frac{\partial \sigma_{ij}}{\partial x_i}-\frac{\partial \bar{p}}{\partial x_i}-\frac{\partial \tau_{ij}}{\partial x_j}, \tag{2}$$

$$\begin{aligned}&\frac{\partial\left(\rho \tilde{h}_s\right)}{\partial t}+\frac{\partial\left(\rho \tilde{u}_i \tilde{h}_s\right)}{\partial x_i}-\frac{\partial \bar{p}}{\partial t}-\bar{u}_j \frac{\partial \bar{p}}{\partial x_i}\\&-\frac{\partial}{\partial x_i}\left(\lambda \frac{\partial \tilde{T}}{\partial x_i}\right)=-\frac{\partial}{\partial x_j}\left[\rho\left(u_i \tilde{h}_s-\tilde{u}_i \tilde{h}_s\right)\right],\end{aligned} \tag{3}$$

where ρ is the density, t is the time, u is the speed, p is the pressure, τ_{ij} is the viscous stress tensor, u_i and u_j are velocity components, h is the enthalpy, λ is the thermal conductivity, and T is the temperature. The transport equation of quantity c after Favre filtration is as follows:

$$\begin{aligned}&\frac{\partial(\rho \tilde{c})}{\partial t}+\nabla \cdot(\rho \tilde{u} \tilde{c})+\nabla[\rho(\widetilde{u c}-\tilde{u} \tilde{c})]\\&=\overline{\nabla \cdot(\rho D \nabla \tilde{c})}+\overline{\dot{\omega}_c},\end{aligned} \tag{4}$$

where D is the diffusion coefficient, $\dot{\omega}_c$ is the normalized chemical reaction rate, obtained according to $\dot{\omega}_c=\frac{S}{HY_{fuel}}$, S is the heat of chemical reaction, H is the calorific value, and Y_{fuel} is the mass fraction of the fuel in the mixture.

To close the equations, a subgrid model is required. In this study, the WALE model was chosen because it can better capture the change of the flow field from laminar to turbulent and is less computationally intensive(Nicoud, 1999). The equation is as follows:

$$\tau_{ij}-\frac{1}{3}\tau_{kk}\delta_{ij}=-2\mu_{sgs}\bar{s}_{ij}. \tag{5}$$

μ_{sgs} is the subgrid viscosity coefficient, defined as follows:

$$\mu_{sgs}=\rho L_s^2\frac{\left(s_{ij}s_{ij}\right)^{3/2}}{\left(\bar{s}_{ij}\bar{s}_{ij}\right)^{3/2}+\left(s_{ij}s_{ij}\right)^{5/4}}, \tag{6}$$

where L_s is the subgrid-scale mixing length, and s_{ij} is the spin rate tensor component.

In addition, in premixed combustion, thickening of the front surface of the flame is required to obtain more accurate calculation results. Therefore, the Zimont model is used in this paper (Zimont & Battaglia, 2005).

2.1 Model Size

The mesh dimensions were kept the same, as in previous studies (Lv et al., 2016), and the experimental procedure is not repeated here. Figure 1 shows the mesh model used and the size details. The model was a tube with a rectangular cross section, and its size was consistent with the description in the literature (Lv et al., 2016). The rectangular section was 100 mm × 100 mm, and the overall length of the tube was 500 mm. The ignition point was set at the center of the rectangular section at the bottom of the tube, and the positive Y-axis direction was the direction of flame propagation. The obstacles were flat types with dimensions of 50 mm × 100 mm × 10 mm, and they were placed 200 mm from the ignition point. The pressure monitoring point was set to 20 mm to the right of

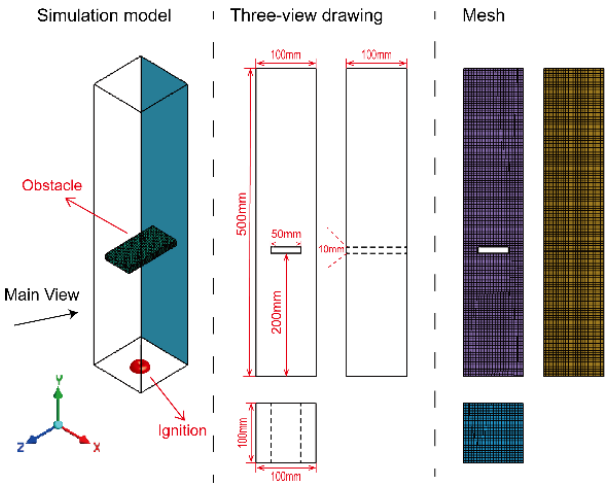

Fig. 1 Simulation model and its size and mesh

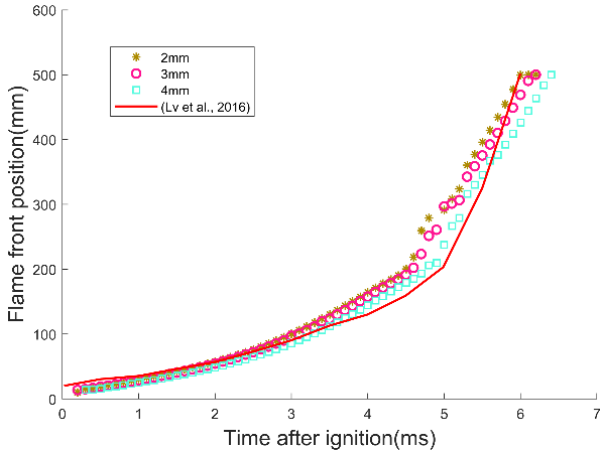

Fig. 3 Comparison of how well the results for three different grids fit the experimental data. The three grid sizes were 2, 3, and 4 mm

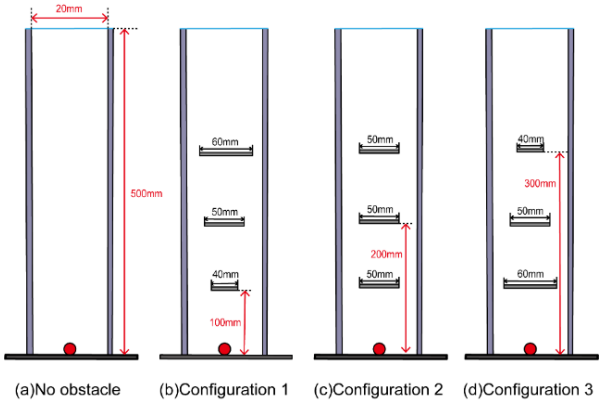

Fig. 2 Four configurations analyzed in this paper. The first is the configuration without obstacles

the ignition point, as shown in Fig. 1. In this paper, the four configurations in Fig. 2 were studied on the basis of this model to analyze the effect of the obstacle length variations on hydrogen deflagration.

2.2 Mesh Division

Figure 1 shows the division of the mesh. In the LES, there is no strict sense of "grid independence verification" and it is better to apply a finer grid as much as possible while balancing the computational accuracy and time cost (Li et al., 2022). However, in practical applications, it is still necessary to check the grid independence to ensure the simulation results agree with the experimental results to the maximum extent. Therefore, based on the independence check shown in Fig. 3, it was found that the 3-mm mesh fit better with the experiment, and considering the arithmetic power and time cost, a 3 mm × 3 mm × 3 mm hexahedral mesh was chosen in this study, with a total of 203,184 mesh elements. Di Sarli et al. (2009) and Chen et al. (2017) also showed in their previous work that this grid resolution is sufficient to simulate the deflagration of combustible gases.

2.3 Numerical Details

The walls of the tube and the surfaces of the obstacles were set to be no-slip. It was worth mentioning that a polyvinyl chloride (PVC) film was used at the outlet to prevent gas spillage, which would cause a rupture under pressure shock and had little effect on the process of deflagration. Therefore, its effect was ignored in this simulation study (Pan et al., 2022a). The specific heat of the unburned and burned mixtures was approximated by piecewise polynomial functions of the temperature. The molecular viscosity was calculated from Sutherland's law of air viscosity (Li et al., 2022a). The fuel was selected as a hydrogen–air mixture with an initial fuel concentration of 25.63% and laminar flame speed from the literature (Xiao et al., 2018).

The wall of the tube was set to be adiabatic. The outlet was set to be non-reflective in order to avoid pressure attenuation caused by pressure wave reflection. The process variable was assigned a value of 1 to realize the ignition (Charlette et al., 2002). The initial temperature was set to 300 K.

Calculations were performed using the Ansys Fluent platform. The SIMPLE algorithm was used to couple the pressure and velocity fields. To ensure the convergence of the calculation results, the time step was set to 1×10^{-6} s in the solver, and 40 iterations were required within each time step.

2.4 Numerical Validation

Figure 4 shows the comparison of the simulated and experimental overpressures. The two curves have similar rise rates, fall rates, and pressure peaks. The locations where there are differences are explained in this section. P_4 corresponded to the wave peak generated when the PVC film was broken by the pressure wave. As this factor was ignored in the simulation, the corresponding wave peak did not appear in the simulated curve (Li et al., 2017, 2021, 2022a, Pan et al., 2022a).

A major advantage of numerical simulations is that they can capture many details that are not available in traditional experiments due to hardware facility limitations, such as P_3 in Fig. 4. P_3 is the crest generated when the flame first came into contact with an obstacle during propagation, which was not evident in the

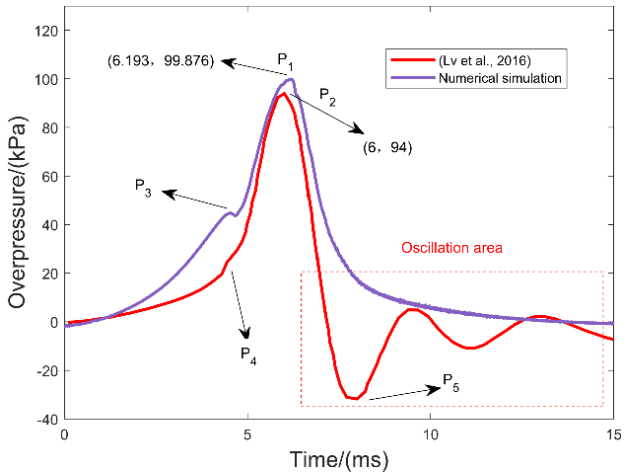

Fig. 4 Comparison of the simulated and experimental overpressures. Special points are labelled as P_1–P_5

experimental curve (Hao et al., 2022). P_1 is the highest point of the experimental pressure and P_2 is the highest point of the simulated pressure. It can be seen that the simulated curve was very close to the experimental curve at the vertices P_1 and P_2, with an error of only 3.2% in time and 6.25% in value for the two pressure points.

P_5 is a negative pressure, which appeared in the experimental curve. Since the outlet was set to no reflection in the simulation, the corresponding negative pressure and the pressure oscillation phase in the final stage did not appear in the simulation curve. This arose in the experiment because when the flame rushed out of the tube, it brought out a large amount of gas, which reduced the amount of gas inside the tube significantly and therefore created a negative pressure. When the outside air was replenished, the pressure was restored. This process was repeated, so an oscillation region at the final stage of the experiment appeared (Wang et al., 2022b). Because the focus of this paper is primarily the process of pressure changes during the deflagration phase and because the pressure is high, the above errors are within an acceptable range.

Figure 5 shows a comparison of the simulated and experimental flame propagation processes. The flame propagation processes had a high degree of similarity. In the early stage of flame propagation, both the simulated and experimental flames propagated forward as spherical flames. At this stage, the structural deformation of the flame and the instability of the flame were very weak. The flame propagated forward in the form of the laminar flow. It then transformed into a finger-shaped flame. The flame was squeezed upon contact with the obstacle, and then it was squeezed into the space channel formed by the sides of the obstacle and the walls of the tube, and symmetric branching flames appeared. Due to the presence of vortices, the two branch flames approached each other toward the centerline of the tube in the area downstream of the obstacle.

The branch flames a' and b' marked by red rectangular boxes in Fig. 5 correspond to the experimental flames a and b, respectively. The simulated flames results showed more details. The simulated section revealed tiny, jagged

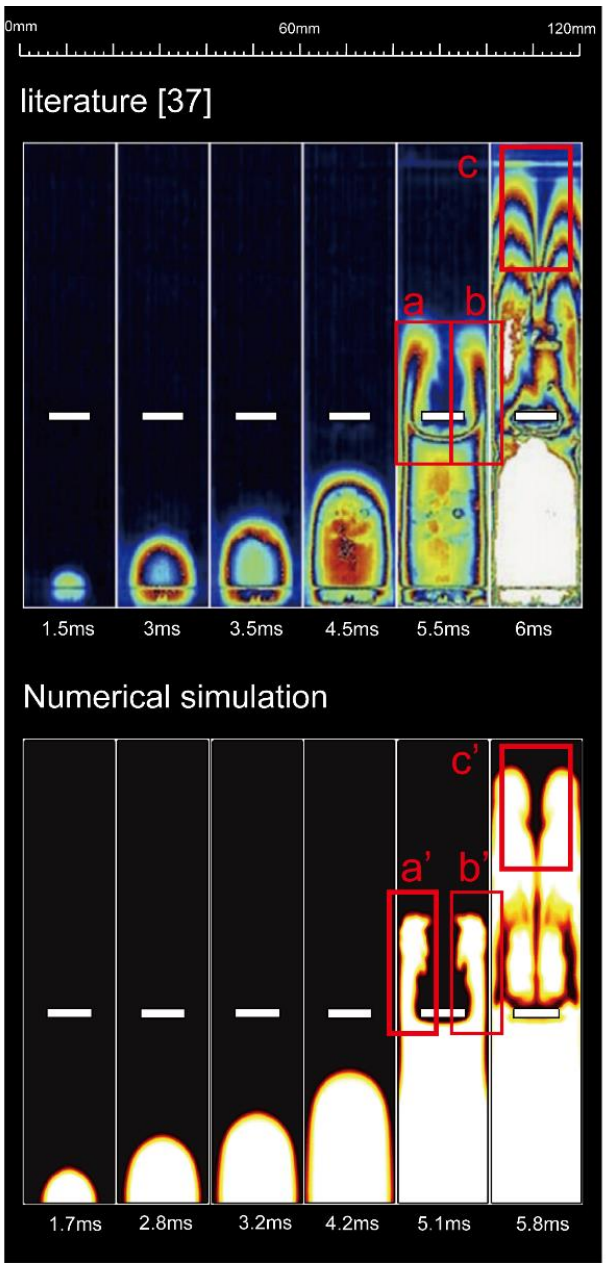

Fig. 5 Comparison of the simulated and experimental flame propagation processes. Corresponding regions are marked with red boxes, such as a and a', b and b', and c and c'

flame deformations on the branching flames, as shown by a'. This was because as the flame traversed the channel formed by the obstacle and the tube wall, it was stretched in the flow direction due to severe flow contraction and pressure waves. The instability produced shear layers and small vortices that attached to the left and right branch flames (Wang et al., 2022b). This deformed flame was only partially captured in the experiment because of the hardware limitations and other factors, as shown by a. Thereafter, the branch flames moved closer together and merged, and the unmerged flames formed a gap in the upper part of the overall flame, as shown by c and c'. When the flame touched the outlet of the tube, the reversed flame also touched the back wall surface of the obstacle and filled this part of the flame cavity. Overall, the combustible

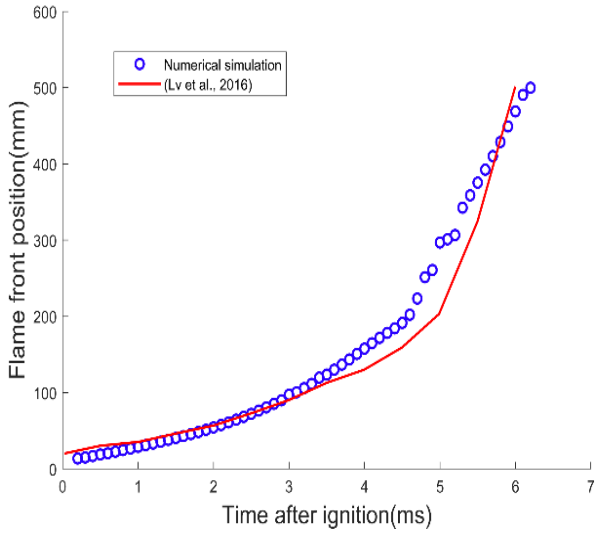

Fig. 6 Comparison of the positions of the flame front surfaces

gases inside the tube were completely burned at the moment the flame rushed out of the tube.

Figure 6 shows the comparison of the positions of the flame front surfaces. There was almost no difference in the overall response times of the simulation and the experiment, and the location of the simulated flame front surface was in good agreement with that of the experiment. As seen in Fig. 6, the simulated flame propagated slightly faster than that in the experiment. This was because the tube wall in the simulation was set to be adiabatic and the heat dissipation was neglected (Guo et al., 2022). Thus, the flame propagation velocity and overpressure were slightly larger those in the experiment.

In summary, after comparing with the experimental overpressure and flame, the model was found to have good reproducibility and predictability. Thus, the model proposed in this paper can be considered to be accurate and efficient.

3. RESULTS AND DISCUSSION

3.1 Flame Propagation Process

Figure 7 shows a comparison of the flame propagation processes for the four configurations. Corresponding moments of the processes were selected when the flame front surfaces were at the same position. Figure 7(a) shows the control case with no obstacles, where it can be seen that the flame first propagated forward in a hemispherical shape and then transformed into a finger shape. At t = 6 ms, the front of the flame started to show a slight change, and the flame front tended to flatten and reverse, which was caused by the inconsistency of the propagation speed between the outer wall surface of the flame and the inner part of the flame (Xiao et al., 2018).

Figurs 7(b), 7(c), and 7(d) show the three configurations investigated in this paper. After ignition, the flame front became flattened when it encountered the first obstacle due to the obstruction of the obstacle and the presence of the unburned gas body. The degree of flattening was influenced by the three different configurations and squeezed the flame into the channels that formed with the tube walls on each side of the obstacle. Due to the vortex, the flame formed a symmetric flame structure after passing through the channel, and the two flames gradually approached the centerline of the tube. At t = 4 ms, the flame formed a symmetric shape that resembled a “French knife” in configurations 1 and 2. However, the lengths of the obstacles in configuration 3 tended to decrease gradually, so the flame formed a thinner branch after the first obstacle. In configuration 3, the flame was already rushing to the next obstacle without being completely close to the centerline. This was because wider flame propagation channels as well as more combustible gases induced the flame to propagate forward rapidly. At the same time, the degree of turbulence of the flame was increasing. Compared to configurations 1 and 2, configuration 3 has a twisted flame shape that resembled “French knife” in the area downstream of the first obstacle.

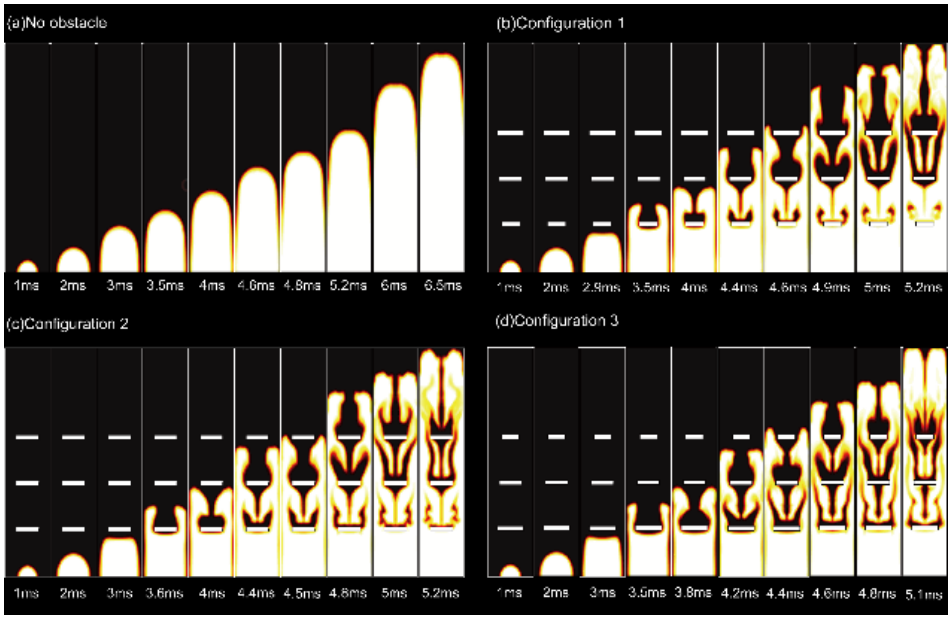

Fig. 7 Comparison of the flame propagation processes for the four configurations

The flame immediately reflected when it approached the obstacle due to the restraining effect of the tube wall and the reflecting effect of the shock wave. The flame was squeezed and then moved around along the sides of the obstacle, and in the process, the contact area between the flame and the obstacle increased, generating an outwardly expanding reflected wave. When the flame passed over the front wall of the obstacle, a shock wave formed around the back wall of the obstacle and drove the unburned gas to form a vortex. At t = 4.4 ms for both configurations 1 and 2 and t = 4.2 ms for configuration 3, the flame passed the second obstacle and started to appear to approach the centerline in the area downstream of the second obstacle. At this point, the flames in the downstream area of the first obstacle appeared to be fused and formed some peculiar flame cavities due to the flames having less energy to maintain the split and rapidly consumed the vortex (Wang et al., 2023). The pressure and turbulence in the tube continued to rise, making the axial velocity of the flame greater than the radial velocity during propagation.

After passing the third obstacle, the flame showed inward rotation as it approached. It may be that the particular shape of the obstacles amplified the vortices of the flow field so that the propagation direction of the flame front surface was reversed after passing the length-varying obstacles (Wen et al., 2013). This phenomenon was evident in configurations 1 and 2. Figure 7 shows the special structure of the front surface of the flame fused with its main flame after internal rotation captured in the area downstream of the third obstacle. The internal rotation structure at the same position in configuration 3 was less pronounced, which was related to the structure with the gradually decreasing lengths of the obstacles. It can be seen that only gradually decreasing the gaps could induce the generation of large scale vortices. The time needed for the flame to reach the end of the tube was essentially the same for all three configurations. It can be seen that the downstream areas of the first obstacles of the three configurations were almost filled with flames after the flames filled the tube. In the regions downstream of the second obstacles, the flames underwent four stages: convergence, internal rotation, stretching, and shedding, and then "goat horn"-like flame cavities formed in these areas. The lengths of the goat horn flame cavities from small to large were as follows: configuration 3, configuration 2, and configuration 1. This indicated that configuration 1 had a significant stretching effect on the propagation of the flame. This same effect resulted in a large rectangular flame cavity in the downstream region of the third obstacle of configuration 1.

3.2 Location and Speed of Flame

Figure 8 shows a comparison of the positions of the front surfaces of the flames. The vertical lines on the horizontal coordinates in Fig. 8 indicate the moments when the flame approached the obstacles in different configurations, and they are distinguished by color. All three obstacle configurations shortened the time taken for the flame to reach the end of the tube, compared to that of the case with no obstacle. Configuration 3 resulted in the shortest time, and the flamed reached the end of the tube in 5.2 ms. The second shortest was configuration 2, with a time of 5.3 ms. The third shortest was configuration 1, with a time of 5.5 ms. The time for the flame to reach the end was 7 ms in the configuration of no obstacle. At the beginning of flame propagation, the flame propagation processes were similar for the four configurations. At t = 2.5 ms, the flames started to show different propagation processes.

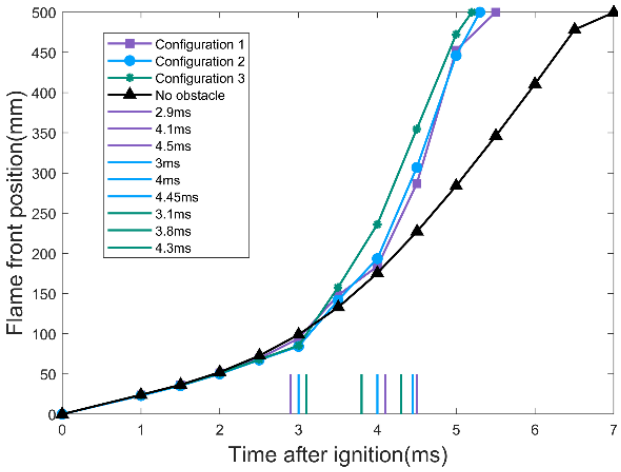

Fig. 8 Comparison of the positions of the front surfaces of the flames

Figure 9 shows a comparison of the propagation speeds of the flames. The propagation speed of the flame was calculated using the following equation:

$$S = \frac{x_{n+1} - x_n}{\Delta t}, \tag{7}$$

where S is the velocity of the flame, $x_{n+1} - x_n$ is the distance between the two flame fronts, and Δt is the time difference between the two flame fronts arriving at the same position.

As can be seen in Fig. 9, there was a significant decrease in the flame propagation speed in the empty tube at the t = 1 ms. The sudden deceleration of the flame was caused by the expansion wave when the flame first came

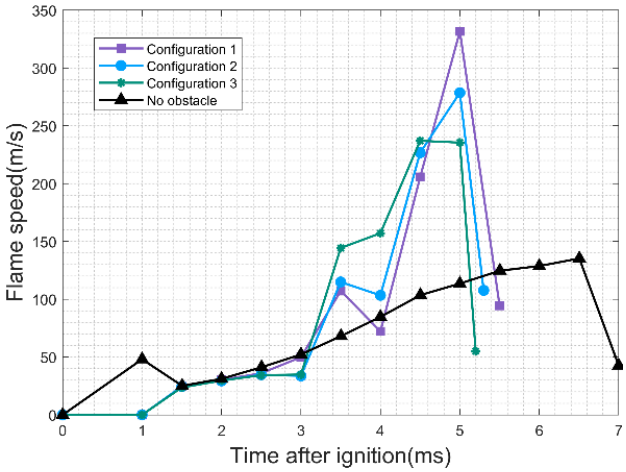

Fig. 9 Comparison of the propagation speeds of the flames

Table 1 Information about flame speeds of four configurations

	A_1 (m/s)	G_1 (%)	A_2 (m/s)	G_2 (%)	S_{max} (m/s)	t_{Max} (ms)
1	50→107	114	72.2→332	360	332	5
2	33.7→115	241	103→279	170.8	279	5
3	34.9→144	312.6	157→237	60	237	4.5
No obstacle	-	-	-	-	135	6.5

in contact with the side wall of the tube, after which it continued rising slowly (Xiao et al., 2018). At t = 3 ms, all three obstacle configurations increased the flame speed, and the flame appeared to accelerate for the first time. The most dramatic growth was seen in configuration 3, where the flame speed increased from 34.9 to 144 m/s, a growth rate of 312.6%. This moment was the time when the flame was close to the first obstacle. This indicated that the obstacle configuration with a gradually decreasing length had a significant acceleration effect in the early stage.

At t = 3.5–4 ms, there was a decrease in the flame speed for both configurations 1 and 2 and a decrease in the growth rate for configuration 3. This was the time for the flame to fuse in the downstream area of the first obstacle. This was because the fusion of the flames in the tube resulted in a lower flame speed. Compared to the case with no change in length, configuration 1 with a gradually increasing length promoted this phenomenon, and configuration 3 with a gradually decreasing length suppressed it.

At t = 4 ms, the three configurations again caused a violent increase in the flame speed, and the flame appeared to accelerate for the second time. For configurations 1 and 2, this flame acceleration was the strongest of the whole flame propagation process. The flame speed of configuration 1 increased from 72.2 to 332 m/s, a growth rate of 360%. This was because the area of the channel gradually became smaller, and the flame was forced by the obstacles into the tiny channels on both sides. At the same time, the gas in the tube was pushed forward by the flame, and the pressure in this part became larger, further increasing the speed of the flame rushing out of the tube. The configuration with gradually increasing lengths of the obstacles had a significant acceleration effect on the flame propagation speed in the later stages, and the acceleration was greater than the first acceleration. The speeds of the flames of all three configurations reached the highest values after the two accelerations. After reaching the maximum, the flame speed started to drop.

The above information is recorded in Table 1. A_1 denotes the first acceleration, and G_1 denotes the growth rate of the first acceleration. A_2 denotes the second acceleration, and G_2 denotes the growth rate of the second acceleration. S_{Max} denotes the maximum speed, and t_{Max} denotes the time of the maximum speed.

3.3 Coupling Relationship Between Flame Area and Flame Speed

Figure 10 shows line chart of the flame areas for the four configurations. For a clearer view, it was converted to a bar chart, which is shown in Fig. 11. Based on the two figures, the flame areas of the four configurations did not differ much in the early stage of flame propagation. The

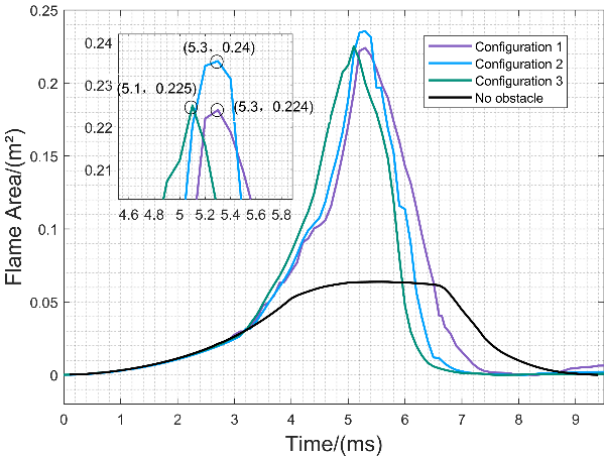

Fig. 10 Line chart of the flame areas for the four configurations

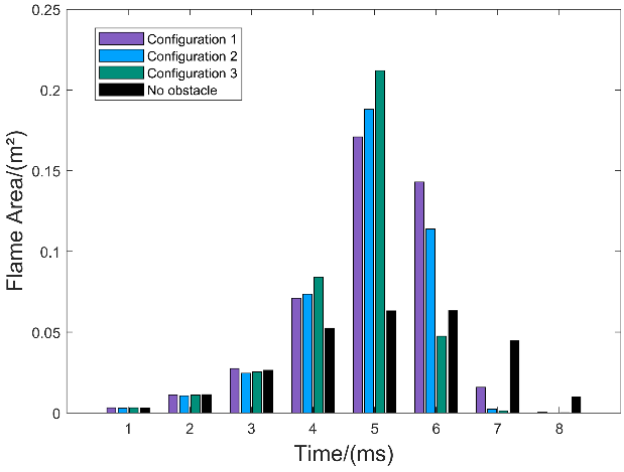

Fig. 11 Bar chart of the flame areas for the four configurations

discrepancy began to appear when the flame approached the first obstacle. At t = 3 ms, the flame area of configuration 3 began to increase significantly, and the rate of increase was greater than those of configurations 1 and 2. As a result, configuration 3 had shortest time to reach the maximum flame area.

Based on Figs. 8 and 9, the flame front of configuration 3 had the shortest time to reach the end of the tube, while the flame speed of configuration 3 had the shortest time to reach its maximum value. The same phenomenon occurred for configurations 1 and 2. This indicated that the flame area and the flame speed had a relationship over time, and the two promoted each other. From Fig. 10, it can be determined that the maximum values of the flame areas for both configurations 1 and 3

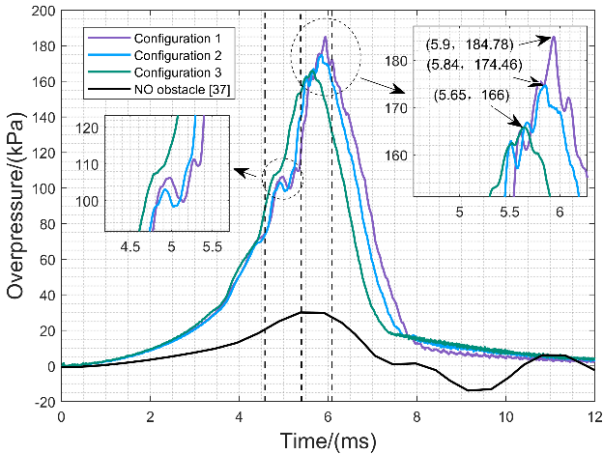

Fig. 12 Comparison of the explosion overpressures of the four configurations. The dotted lines divide time into three parts

were smaller than that of configuration 2. This indicated that the flame area was suppressed when the lengths of the obstacles were varied because the complex wall conditions increased the turbulence intensity of the flame, causing some of the flame to fall off or be extinguished.

3.4 Comparative Analysis of Explosion Overpressure

Figure 12 shows the comparison of the explosion overpressures of the four configurations. The overpressure of the configuration with obstacles was significantly higher than that of the case without obstacles. The entire pressure curve can be divided into four parts. The first part is a steady rise phase, the second phase is a local peak phase, the third phase is a rapid growth phase, and the fourth phase is a rapid decline phase.

In the steady rise phase, deflagration was in the initial stage. When the reaction rate was small, the pressure, temperature, and other parameters were low, and the pressure curve did not have significant variability. Differences in the pressure curves began to appear during the local peak phase, with different structures creating different slopes and peaks in the pressure curve. This was due to the variation in the lengths of the obstacle as well as the wall of the tube causing the pressure waves to propagate in different ways. Complex reflected and diffracted waves appeared in a narrow tube, and the reflected and diffracted waves were superimposed in a specific area to produce a local high-pressure area. In addition, the change in the flame morphology is an important reason for the appearance of local pressure peaks. In the rapid growth phase, when the reaction rate in the tube reached its maximum, the reaction was violent, and the slope of the pressure curve reached its maximum. During the rapid decline phase, the combustible gases were consumed, heat was dissipated in large quantities, and the pressure in the confined space was rapidly reduced.

As shown Fig. 12, configuration 3 required the shortest time to reach the maximum overpressure (5.65 ms), configuration 2 was in the middle (5.84 ms), and configuration 1 required the longest time (5.9 ms). Based on these results and those in Fig. 10, the time to reach the maximum overpressure lagged slightly behind the time when the flame area reached its maximum value, which was due to the surge generated by the flame combustion that promoted the rise of the overpressure (Li et al., 2022b).

All three configurations where obstacles were present significantly increased the overpressure. Compared with configuration 2, configuration 1 promoted the increase in the pressure with a growth rate of 5.92%, and configuration 3 had a suppressive effect on the pressure with a decrease rate of 4.85%. This indicated that the overpressure of hydrogen deflagration increased when the obstacle length increased gradually, while the overpressure of hydrogen deflagration decreased when the obstacle length decreased gradually. This was because the configuration affected the turbulence intensity of the flame, which changed the crease area of the flame and also complicated the wall conditions, which affected the propagation of the pressure wave and thus the overpressure.

In addition, pressure fluctuations were observed in the local peak phase from t = 4.5–5.5 ms for all three configurations with obstacles. Two peaks appeared in configuration 1, one appeared in configuration 2, and no significant peaks were produced in configuration 3, but there was a transient decrease in the pressure growth rate in configuration 3. Based on these results and those in Fig. 7, it can be seen that t = 4.5–5.5 ms was the period when the flame passed through the third obstacle and produced fusion in its downstream area. As shown in Fig. 7, two flame internal rotations were formed in the downstream region of the third obstacle of configuration 1, one flame internal rotation appeared in this region for configuration 2, and no significant flame internal rotation was produced in this region for configuration 3. This suggested that the number of flame internal rotations may have been positively correlated with the local peak generated during the overpressure rise process. Because the area of the flame had a positive feedback relationship with the overpressure and the flame produced internal rotation while instantly increasing the area of the flame, a corresponding change occurred.

Information about the overpressure is presented in Table 2. P_{Max} is the maximum overpressure. G_{Max}_1 is the growth rate of the maximum overpressure (relative to that of the case with no obstacle). t_{max} is the time of maximum overpressure. G_{Max}_2 is the growth rate of maximum overpressure (relative to that of configuration 2).

3.5 Coupling Relationship Between Flame, Overpressure, and Flow Field

Figure 13 shows the coupling relationship of the flame, overpressure, and flow field for the three obstacle configurations. The background color reflects the distribution of pressure at the current moment, the black contour line is the flame boundary, and the white line is the flow line formed by the tangent of the velocity vector.

During the flame propagation, the overpressure peak appeared mostly at the moment of flame fusion, as shown by the black rectangular dashed boxes labelled c, d, e, and

Table 2 Information about overpressures of four configurations.

Configuration	P_{max} (kPa)	G_{Max}_1 (%)	t_{Max} (ms)	G_{Max}_2 (%)
1	184.78	513.89	5.90	5.92
2	174.46	479.60	5.84	-
3	166.00	451.50	5.65	-4.85
No obstacle	30.10	-	5.38	-

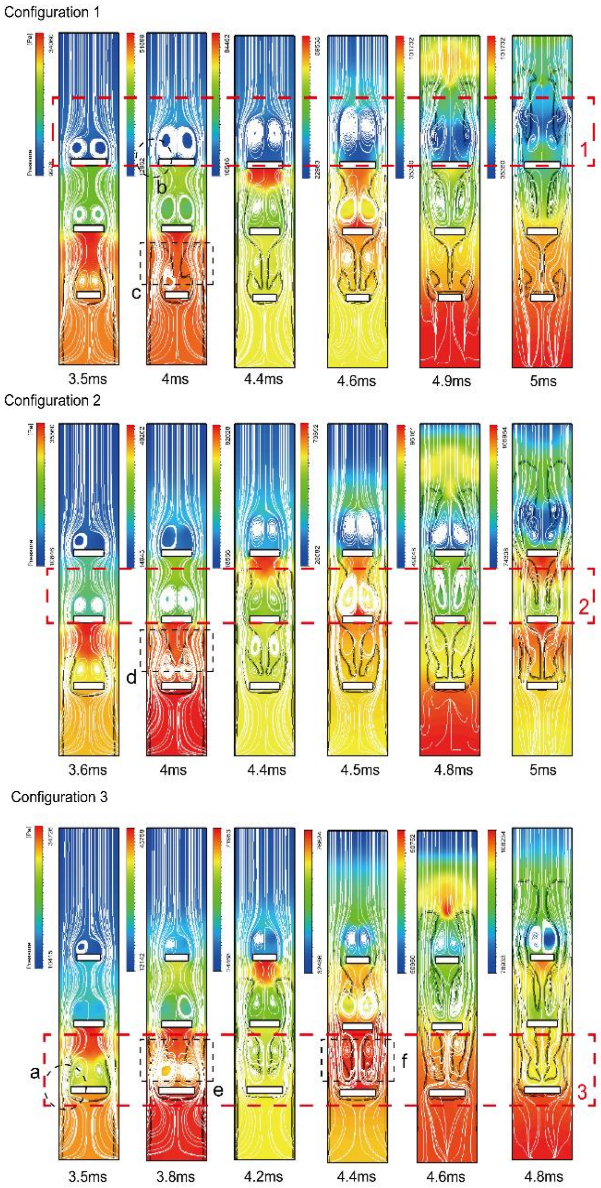

Fig. 13 Coupling relationships of the flame, overpressure, and flow field for the three obstacle configurations. Some special locations are marked

f, which is consistent with the results described in Section 3.4 and with the conclusions obtained and with the conclusions obtained in a previous study (Lv et al., 2016).

After the flame passed the second obstacle, a localized area of high pressure formed between the propagation front of the flame and the third obstacle. The extension of this high-pressure area varied depending on the configuration. The reason for the formation was that the unburned gas body was pressurized by the pressure wave and accumulated at the obstacle walls, and a high pressure formed due to thermal expansion. At the same time, the flame front served as a boundary to split the gas in the region into low-density combustion products and high-density unburned gas bodies, which triggered Rayleigh–Taylor (R-T) and Kelvin–Helmholtz (K-H) instabilities under the shear force of the high-speed flowing gas. The instability intensified the degree of turbulence in the flow field, which further enlarged the scale of the vortex. Due to the vortex coiling effect, the branching flames fused, while the crease area of the flame increased and the overpressure rose further.

At t > 4.5 ms, the vortices of all three configurations reached their maximum, and the degree of turbulence increased further. Due to the differences in the configurations, the positions and development processes of the vortices in the three configurations were different.

Box 3 indicates the location downstream of the first obstacle. Box 2 indicates the location downstream of the second obstacle. Box 1 shows the position downstream of the third obstacle. The vortices of configuration 1 underwent four stages of expansion, acceleration, movement (exit direction), and disappearance in the time period of t = 3.5–5 ms, as shown in the red box labelled 1. The vortices of configuration 2 underwent five stages of acceleration, deceleration, expansion, stretching, and disappearance during the period of t = 3.6–4.8 ms, as shown in the red box labelled 2. The vortices of configuration 3 underwent five stages of acceleration, expansion, fusion, stretching, and disappearance at t = 3.5–4.8 ms, as shown in the red marked labelled 3.

After the flame passed through the obstacle, the surge generated by the burning flame disturbed the flow field in the tube and formed vortices of different degrees downstream. The first obstacle of configuration 3 had the largest length dimension and the resulting channel stretched the flame (Chen et al., 2020), where the flow lines were also the densest, as shown by marker a. The flame was accelerated through the obstacle, and the velocity change is reflected in Fig. 9 for configuration 3 at t = 3–3.5 ms for flame acceleration. However, the flame branches were thin, and the flame had little effect on the flow field in the downstream region of the obstacle, so no significant vortices formed. The passage of configuration 1 gradually decreased, and the streamlines became denser. Finally, the densest region appeared at t = 4 ms, as shown by marker b. These dense streamers are responsible for the flame acceleration of configuration 1 at t = 4–5 ms, as shown in Fig. 9.

Configuration 1 amplified the vortices of the flow field, which was the main reason for the maximum flame propagation speed in configuration 1. The vortex achieved rapid propagation of the flame when rupture occurred.

When the combustible gas produced rotation, the pressure at the center of the rotation was lower than the environmental pressure. When combustion occurred, the pressure at the center of the rotation of the combustible gas began to increase until it approached the environmental pressure due to the decrease in density. At this point, there was a gradient change in the pressure at the center of rotation, and this pressure gradient change led to rapid movement of the combustion gases, which ultimately led to an increase in the flame propagation speed.

4. CONCLUSIONS

In this paper, the effect of the flame structure, flame propagation process, and overpressure characteristics of hydrogen gas after deflagration in a confined space with obstacles was investigated first based on experiments and then using the LES method for simulations. The research results provide a theoretical basis for the prevention and management of hydrogen explosions in narrow spaces, such as various types of pipe corridors, reference suggestions for the placement of various types of equipment and facilities, and guidance for the actual occurrence and development of hydrogen explosion accidents. The results are as follows.

1. The configuration of the obstacles with gradually increasing lengths amplified the vortices in the flow field so that the propagation direction of the flame front surface was reversed after passing three obstacles. This was related to the structures of the obstacles, where gradually decreasing gaps induced the generation of large-scale vortices.

2. The configuration with gradually decreasing lengths of the obstacles had a significant acceleration effect on the flame propagation speed in the early stage, with a growth rate of 312.6%. The configuration with a gradually increasing length of the obstacles had a significant acceleration effect on the propagation speed of the flame in the later stage, with a growth rate of 360%, and it was higher than the first acceleration in the early stage.

3. The particular shapes of the obstacles with gradually increasing lengths amplified the vortices of the flow field, which was the main reason for the maximum speed of flame propagation. Vortices achieved rapid flame propagation when rupture occurred. The change in the pressure gradient that occurred at the center of the rotation caused rapid movement of the combustion gases, which ultimately led to an increase in the flame propagation speed.

4. A configuration with gradually increasing lengths of the obstacles promoted the overpressure, with a growth rate of 5.92%. A configuration with gradually decreasing lengths of the obstacles suppressed the overpressure, with a decrease rate of 4.85%.

5. The reason for the formation of a local high-pressure area was that unburned gas accumulated there due to pressure waves and the obstacle walls, and then its thermal expansion formed a high pressure. The R-T and K-H instabilities caused the overpressure to rise further.

ACKNOWLEDGMENTS

This research was funded by THE BASIC PUBLIC WELFARE RESEARCH PROJECT OF ZHEJIANG PROVINCE, grant number LGF22E040002.

We thank LetPub (www.letpub.com) for its linguistic assistance during the preparation of this manuscript.

CONFLICT OF INTEREST

The authors declare that they have no known competing financial interests or personal relationships that could have appeared to influence the work reported in this paper.

AUTHOR CONTRIBUTIONS

Bingjian Ai developed the numerical model, conducted the simulations, wrote the manuscript, and prepared all the figures. **Jianfeng Gao** supervised and guided the work with his advice due to his long experience in this field. **Jianjun Liang** provided the software. Finally, **Bin Hao** and **Bingang Guo** reviewed and revised the manuscript before submission.

REFERENCES

Ballossier, Y., Virot, F., & Melguizo-Gavilanes, J. (2021). Flame propagation and acceleration in narrow channels: Sensitivity to facility specific parameters. *Shock Waves*, *31*(4), 307-321. https://doi.org/10.1007/s00193-021-01015-9

Boeck, L. R., Berger, F. M., Hasslberger, J., & Sattelmayer, T. (2016). Detonation propagation in hydrogen–air mixtures with transverse concentration gradients. *Shock Waves*, *26*(2), 181-192. https://doi.org/10.1007/s00193-015-0598-8

Brennan, S. L., Makarov, D. V., & Molkov, V. (2009). LES of high pressure hydrogen jet fire. *Journal of Loss Prevention in the Process Industries*, *22*(3), 353-359. https://doi.org/https://doi.org/10.1016/j.jlp.2008.12.007

Charlette, F., Meneveau, C., & Veynante, D. (2002). A power-law flame wrinkling model for LES of premixed turbulent combustion Part I: non-dynamic formulation and initial tests. *Combustion and Flame*, *131*(1), 159-180. https://doi.org/https://doi.org/10.1016/S0010-2180(02)00400-5

Chen, C. k., Zhang, Y. l., Zhao, X. l., Lei, P., & Nie, Y. l. (2020). Experimental study on the influence of obstacle aspect ratio on ethanol liquid vapor deflagration in a narrow channel. *International Journal of Thermal Sciences*, *153*, 106354. https://doi.org/https://doi.org/10.1016/j.ijthermalsci.2020.106354

Chen, P., Sun, Y., Li, Y., & Luo, G. (2017). Experimental and LES investigation of premixed methane/air flame propagating in an obstructed chamber with two slits.

Journal of Loss Prevention in the Process Industries, *49*, 711-721. https://doi.org/https://doi.org/10.1016/j.jlp.2016.11.005

Dai, Q., Zhang, S., Zhang, S., Sun, H., & Huang, M. (2021). Large eddy simulation of premixed CH4/Air deflagration in a duct with obstacles at different heights. *ACS Omega*, *6*(41), 27140-27149. https://doi.org/10.1021/acsomega.1c03814

Debnath, P., & Pandey, K. M. (2023a). Numerical analysis on detonation wave and combustion efficiency of pulse detonation combustor with U-Shape combustor. *Journal of Thermal Science and Engineering Applications*, *15*(10). https://doi.org/10.1115/1.4062702

Debnath, P., & Pandey, K. M. (2023b). Numerical studies on detonation wave in hydrogen-fueled pulse detonation combustor with shrouded ejector. *Journal of the Brazilian Society of Mechanical Sciences and Engineering*, *45*(2), 104. https://doi.org/10.1007/s40430-023-04036-w

Demir, M. E., & Dincer, I. (2018). Cost assessment and evaluation of various hydrogen delivery scenarios. *International Journal of Hydrogen Energy*, *43*(22), 10420-10430. https://doi.org/https://doi.org/10.1016/j.ijhydene.2017.08.002

Di Lullo, G., Giwa, T., Okunlola, A., Davis, M., Mehedi, T., Oni, A. O., & Kumar, A. (2022). Large-scale long-distance land-based hydrogen transportation systems: A comparative techno-economic and greenhouse gas emission assessment. *International Journal of Hydrogen Energy*, *47*(83), 35293-35319. https://doi.org/https://doi.org/10.1016/j.ijhydene.2022.08.131

Di Sarli, V., Di Benedetto, A., & Russo, G. (2009). Using large eddy simulation for understanding vented gas explosions in the presence of obstacles. *Journal of Hazardous Materials*, *169*(1), 435-442. https://doi.org/https://doi.org/10.1016/j.jhazmat.2009.03.115

Dincer, I., & Acar, C. (2015). Review and evaluation of hydrogen production methods for better sustainability. *International Journal of Hydrogen Energy*, *40*(34), 11094-11111. https://doi.org/https://doi.org/10.1016/j.ijhydene.2014.12.035

Elshimy, M., Ibrahim, S., & Malalasekera, W. (2021). LES – DFSD modelling of vented hydrogen explosions in a small-scale combustion chamber. *Journal of Loss Prevention in the Process Industries*, *72*, 104580. https://doi.org/https://doi.org/10.1016/j.jlp.2021.104580

Faye, O., Szpunar, J., & Eduok, U. (2022). A critical review on the current technologies for the generation, storage, and transportation of hydrogen. *International Journal of Hydrogen Energy*, *47*(29), 13771-13802. https://doi.org/https://doi.org/10.1016/j.ijhydene.2022.02.112

Gao, J. F., Ai, B. J., Hao, B., Guo, B. G., Hong, B. Y., & Jiang, X. S. (2022). Effect of obstacles gradient arrangement on non-uniformly distributed LPG-Air Premixed gas deflagration. *Energies*, *15*(19), 6872. https://doi.org/10.3390/en15196872

Gong, Y., & Li, Y. (2018). STAMP-based causal analysis of China-Donghuang oil transportation pipeline leakage and explosion accident. *Journal of Loss Prevention in the Process Industries*, *56*. https://doi.org/10.1016/j.jlp.2018.10.001

Goodwin, G. B., Houim, R. W., & Oran, E. S. (2016). Effect of decreasing blockage ratio on DDT in small channels with obstacles. *Combustion and Flame*, *173*, 16-26. https://doi.org/https://doi.org/10.1016/j.combustflame.2016.07.029

Guo, B., Gao, J., Hao, B., Ai, B., Hong, B., & Jiang, X. (2022). Experimental and numerical study on the explosion dynamics of the non-uniform liquefied petroleum gas and air mixture in a channel with mixed obstacles. *Energies*, *15*(21), 7999. https://doi.org/10.3390/en15217999

Hao, B., Gao, J. F., Guo, B. G., Ai, B. J., Hong, B. Y., & Jiang, X. S. (2022). Numerical simulation of premixed methane-air explosion in a closed tube with U-Type obstacles. *Energies*, *15*(13), 4909. https://doi.org/10.3390/en15134909

Hong, S., Lee, W., Kang, S., & Song, H. H. (2015). Analysis of turbulent diffusion flames with a hybrid fuel of methane and hydrogen in high pressure and temperature conditions using LES approach. *International Journal of Hydrogen Energy*, *40*(35), 12034-12046. https://doi.org/https://doi.org/10.1016/j.ijhydene.2015.05.081

Ji, T., Qian, X., Yuan, M., Wang, D., He, J., Xu, W., & You, Q. (2017). Case study of a natural gas explosion in Beijing, China. *Journal of Loss Prevention in the Process Industries*. https://doi.org/10.1016/j.jlp.2017.07.013

Korytchenko, K., Senderowski, C., Samoilenko, D., Poklonskiy, E., Varshamova, I., & Maksymov, A. (2022). Numerical analysis of the spark channel expansion in a high-pressure hydrogen-oxygen mixture and in nitrogen. *Shock Waves*, *32*(4), 321-335. https://doi.org/10.1007/s00193-022-01077-3

Li, G. Q., Du, Y., Wang, S. M., Qi, S., Zhang, P. L., & Chen, W. Z. (2017). Large eddy simulation and experimental study on vented gasoline-air mixture explosions in a semi-confined obstructed pipe. *Journal of Hazardous Materials*, *339*, 131-142. https://doi.org/10.1016/j.jhazmat.2017.06.018

Li, G. Q., Wu, J., Wang, S. M., Bai, J., Wu, D. J., & Qi, S. (2021). Effects of gas concentration and obstacle location on overpressure and flame propagation characteristics of hydrocarbon fuel-air explosion in a

semi-confined pipe. *Fuel*, *285*, 119268. https://doi.org/10.1016/j.fuel.2020.119268

Li, G., Zheng, K., Wang, S., & Chen, W. (2022a). Comparative study on explosion characteristics of hydrogen and gasoline vapor in a semi-confined pipe based on Large Eddy Simulation. *Fuel*, *328*, 125334. https://doi.org/https://doi.org/10.1016/j.fuel.2022.125334

Li, M., Liu, D., Shen, T., Sun, J., & Xiao, H. (2022b). Effects of obstacle layout and blockage ratio on flame acceleration and DDT in hydrogen-air mixture in a channel with an array of obstacles. *International Journal of Hydrogen Energy*, *47*(8), 5650-5662. https://doi.org/https://doi.org/10.1016/j.ijhydene.2021.11.178

Li, X., Dong, J., Jin, K., Duan, Q., Sun, J., Li, M., & Xiao, H. (2022c). Flame acceleration and deflagration-to-detonation transition in a channel with continuous triangular obstacles: Effect of equivalence ratio. *Process Safety and Environmental Protection*, *167*, 576-591. https://doi.org/https://doi.org/10.1016/j.psep.2022.09.033

Li, Y., Xie, H., Bi, M., Bo, Y., & Gao, W. (2022d). Effects of cloud size and built-in obstacles on hydrogen cloud explosion using large eddy simulation. *Journal of Loss Prevention in the Process Industries*, *77*, 104788. https://doi.org/https://doi.org/10.1016/j.jlp.2022.104788

Liu, J., & Wang, H. (2022). Machine learning assisted modeling of mixing timescale for LES/PDF of high-Karlovitz turbulent premixed combustion. *Combustion and Flame*, *238*, 111895. https://doi.org/https://doi.org/10.1016/j.combustflame.2021.111895

Luo, Z. M., Kang, X. F., Wang, T., Su, B., Cheng, F. M., & Deng, J. (2021). Effects of an obstacle on the deflagration behavior of premixed liquefied petroleum gas-air mixtures in a closed duct. *Energy*, *234*, Article 121291. https://doi.org/10.1016/j.energy.2021.121291

Lv, X., Zheng, L., Zhang, Y., Yu, M., & Su, Y. (2016). Combined effects of obstacle position and equivalence ratio on overpressure of premixed hydrogen–air explosion. *International Journal of Hydrogen Energy*, *41*(39), 17740-17749. https://doi.org/https://doi.org/10.1016/j.ijhydene.2016.07.263

Nicoud, F. D. F. (1999). Subgrid-Scale stress modelling based on the square of the velocity gradient tensor. *Flow, Turbulence and Combustion*, *62(3)*, 183-200. https://doi.org/10.1023/A:1009995426001

Pan, C., Sun, H., Zhu, X., Zhao, J., Wang, X., & Liu, Y. (2022a). Vented ethanol-gasoline vapor explosions initiated by two symmetric sparks in a channel. *Fuel*, *329*, 125499. https://doi.org/https://doi.org/10.1016/j.fuel.2022.125499

Pan, C., Wang, X., Sun, H., Zhu, X., Zhao, J., Fan, H., & Liu, Y. (2022b). Large-eddy simulation and experimental study on effects of single-dual sparks positions on vented explosions in a channel. *Fuel*, *322*, 124282. https://doi.org/https://doi.org/10.1016/j.fuel.2022.124282

Qiming, X., Guohua, C., Qiang, Z., & Shen, S. (2022). Numerical simulation study and dimensional analysis of hydrogen explosion characteristics in a closed rectangular duct with obstacles. *International Journal of Hydrogen Energy*, *47*(92), 39288-39301. https://doi.org/https://doi.org/10.1016/j.ijhydene.2022.09.091

Qin, Y., & Chen, X. (2021). Flame propagation of premixed hydrogen-air explosion in a closed duct with obstacles. *International Journal of Hydrogen Energy*, *46*(2), 2684-2701. https://doi.org/https://doi.org/10.1016/j.ijhydene.2020.10.097

Qin, Y., & Chen, X. (2022). Study on the dynamic process of in-duct hydrogen-air explosion flame propagation under different blocking rates. *International Journal of Hydrogen Energy*, *47*(43), 18857-18876. https://doi.org/https://doi.org/10.1016/j.ijhydene.2022.04.004

Sha, S., Chen, Z., & Jiang, X. (2014). Influences of obstacle geometries on shock wave attenuation. *Shock WaveS*, *24*(6), 573-582. https://doi.org/10.1007/s00193-014-0520-9

Shen, X., Shen, J., Liu, H., Wen, J. X., Ma, Y., Zou, X., & Liu, Z. (2023). Numerical investigation on dynamic behavior of premixed hydrogen/air flame propagation in a closed tube. *Fuel*, *354*, 129295. https://doi.org/https://doi.org/10.1016/j.fuel.2023.129295

Sheng, Z., Yang, G., Gao, W., Li, S., Shen, Q., & Sun, H. (2023). Study on the dynamic process of premixed hydrogen-air deflagration flame propagating in a closed space with obstacles. *Fuel*, *334*, 126542. https://doi.org/https://doi.org/10.1016/j.fuel.2022.126542

Wang, H., Tong, Z., Zhou, G., Zhang, C., Zhou, H., Wang, Y., & Zheng, W. (2022a). Research and demonstration on hydrogen compatibility of pipelines: a review of current status and challenges. *International Journal of Hydrogen Energy*, *47*(66), 28585-28604. https://doi.org/https://doi.org/10.1016/j.ijhydene.2022.06.158

Wang, Q., Luo, X. J., Li, Q., Rui, S. C., Wang, C. J., & Zhang, A. F. (2022b). Explosion venting of hydrogen-air mixture in an obstructed rectangular tube. *Fuel*, *310*, Article 122473. https://doi.org/10.1016/j.fuel.2021.122473

Wang, S., Xiao, G., Mi, H., Feng, Y., & Chen, J. (2023). Experimental and numerical study on flame fusion behavior of premixed hydrogen/methane explosion with two-channel obstacles. *Fuel*, *333*, 126530.

https://doi.org/https://doi.org/10.1016/j.fuel.2022.126530

Wang, T., Yang, P., Yi, W., Luo, Z., Cheng, F., Ding, X., Kang, X., Feng, Z., & Deng, J. (2022c). Effect of obstacle shape on the deflagration characteristics of premixed LPG-air mixtures in a closed tube. *Process Safety and Environmental Protection*, *168*, 248-256. https://doi.org/https://doi.org/10.1016/j.psep.2022.09.079

Wen, X., Ding, H., Su, T., Wang, F., Deng, H., & Zheng, K. (2017). Effects of obstacle angle on methane–air deflagration characteristics in a semi-confined chamber. *Journal of Loss Prevention in the Process Industries*, *45*, 210-216. https://doi.org/https://doi.org/10.1016/j.jlp.2017.01.007

Wen, X., Yu, M., Liu, Z., Li, G., Ji, W., & Xie, M. (2013). Effects of cross-wise obstacle position on methane–air deflagration characteristics. *Journal of Loss Prevention in the Process Industries*, *26*(6), 1335-1340. https://doi.org/https://doi.org/10.1016/j.jlp.2013.08.006

Xiao, G. Q., Wang, S., Mi, H. F., & Khan, F. (2022). Analysis of obstacle shape on gas explosion characteristics. *Process Safety and Environmental Protection*, *161*, 78-87. https://doi.org/10.1016/j.psep.2022.03.019

Xiao, H., Duan, Q., Jiang, L., & Sun, J. (2014a). Effects of ignition location on premixed hydrogen/air flame propagation in a closed combustion tube. *International Journal of Hydrogen Energy*, *39*(16), 8557-8563. https://doi.org/https://doi.org/10.1016/j.ijhydene.2014.03.164

Xiao, H., Duan, Q., & Sun, J. (2018). Premixed flame propagation in hydrogen explosions. *Renewable and Sustainable Energy Reviews*, *81*, 1988-2001. https://doi.org/https://doi.org/10.1016/j.rser.2017.06.008

Xiao, H., Sun, J., & Chen, P. (2014b). Experimental and numerical study of premixed hydrogen/air flame propagating in a combustion chamber. *Journal of Hazardous Materials*, *268*, 132-139. https://doi.org/https://doi.org/10.1016/j.jhazmat.2013.12.060

Xiao, H., wang, Q., Shen, X., Guo, S., & Sun, J. (2013). An experimental study of distorted tulip flame formation in a closed duct. *Combustion and Flame*, *160*(9), 1725-1728. https://doi.org/https://doi.org/10.1016/j.combustflame.2013.03.011

Zhao, B., Li, S., Gao, D., Xu, L., & Zhang, Y. (2022). Research on intelligent prediction of hydrogen pipeline leakage fire based on Finite Ridgelet neural network. *International Journal of Hydrogen Energy*, *47*(55), 23316-23323. https://doi.org/https://doi.org/10.1016/j.ijhydene.2022.05.124

Zhou, Y., Li, Y., & Gao, W. (2023). Experimental investigation on unconfined hydrogen explosion with different ignition height. *International Journal of Hydrogen Energy*. https://doi.org/https://doi.org/10.1016/j.ijhydene.2023.02.072

Zimont, V. L., & Battaglia, V. (2005). Joint RANS/LES approach to premixed flames modelling in the context of the TFC combustion model. *Engineering Turbulence Modelling and Experiments 6*, *77*(1-4), 905-914. https://doi.org/10.1016/B978-008044544-1/50087-X